J. Appl. Comput. Mech., 12(3) (2026) 1093-1105
DOI: 10.22055/jacm.2025.48336.5158

ISSN: 2383-4536
jacm.scu.ac.ir

Shahid Chamran University of Ahvaz

Journal of Applied and Computational Mechanics

Research Paper

Investigation of Pulsatile Blood Flow Dynamics in Anterior Cerebral Artery Aneurysms under Different Physiological Conditions: Hemodynamic Analyses

Mostafa Barzegar Gerdroodbary[1,2], Li-Cai Zhao[3]

[1] Department of Mechanical Engineering, Iranian Research Organization for Science and Technology (IROST), Tehran, Iran, Email: mbarzegarg@yahoo.com

[2] Department of Electromechanical Engineering, C-MAST-Center for Mechanical and Aerospace Science and Technology, Universidade da Beira Interior, Covilha, Portugal, Email: m.barzegargerdroodbary@ubi.pt

[3] School of Mechanical Engineering, Tianjin University, Tianjin, China, Email: river1364@outlook.com

Received April 04 2025; Revised December 07 2025; Accepted for publication December 22 2025.
✉ Corresponding author: M. Barzegar Gerdroodbary (mbarzegarg@yahoo.com); L. Zhao (river1364@outlook.com)

Abstract. This computational study investigates how sac volume influences rupture risk in anterior cerebral artery (ACA) aneurysms under different physiological conditions. Three representative body states—rest, normal activity, and sport—are modeled to quantify their effects on key hemodynamic parameters associated with aneurysm stability. Patient-specific geometries are simulated using the transient Navier–Stokes equations with the Casson non-Newtonian model to accurately capture the shear-thinning behavior of blood. Wall shear stress (WSS) and oscillatory shear index (OSI) are evaluated throughout the cardiac cycle to characterize flow-induced mechanical loading on the aneurysm wall. The results demonstrate that although larger aneurysms exhibit higher internal velocities, their broader ostium areas distribute inflow more uniformly, producing smaller localized high-risk regions. In contrast, smaller aneurysms experience sharply concentrated WSS at the ostium due to restricted inflow, generating focal zones of elevated mechanical fatigue that may predispose them to rupture. The dome of large aneurysms remains the dominant high-pressure and high-WSS region, whereas the neck region governs rupture-related stress patterns in small aneurysms. Furthermore, while changes in body physiology significantly alter flowrate and WSS magnitudes, OSI values in large aneurysms remain relatively stable, indicating reduced susceptibility to oscillatory flow disturbances. These findings highlight the coupled roles of sac volume and physiological state in shaping aneurysm hemodynamics and provide improved mechanistic insight into size-dependent rupture risk.

Keywords: Cerebral aneurysms; Blood hemodynamic; CFD; Body physiology; Non-Newtonian flow.

1. Introduction

Understanding the intricate relationship between body physiology and hemodynamics is crucial in the study of Anterior Cerebral Artery (ACA) aneurysms. The ACA, a key component of the brain's vascular system, is susceptible to the formation of aneurysms, which are abnormal bulges or "ballooning" in the walls of blood vessels. The rupture of these aneurysms can lead to life-threatening conditions such as subarachnoid haemorrhage [1, 2]. The risk of rupture is influenced by various factors, including the size of the aneurysm sac and the stage of the cardiac cycle. Small and giant aneurysms pose different challenges and risks. Small aneurysms, despite their size, should not be underestimated as they can still rupture and cause significant damage. On the other hand, giant aneurysms, due to their large sac volume, have a higher risk of rupture and can lead to more severe consequences [3, 4]. The cardiac cycle, which includes all the physiological processes from the beginning of one heartbeat to the next, plays a significant role in the hemodynamics of ACA aneurysms. Different stages of the cardiac cycle, such as systole and diastole, can affect blood flow patterns and pressures within the aneurysm sac, thereby influencing the rupture risk [5].

Computational Fluid Dynamics (CFD) provides a powerful tool for investigating these complex interactions. By simulating blood flow within the aneurysm sac, CFD can offer valuable insights into the hemodynamic aspects of ACA aneurysms. This approach can help in predicting rupture risk and informing clinical decision-making, ultimately contributing to improved patient outcomes [6-8]. In conclusion, the interplay between body physiology, hemodynamics, and ACA aneurysms is a complex but vital area of study. Through advanced techniques like CFD, we can enhance our understanding and management of ACA aneurysms, paving the way for more effective and personalized treatment strategies [9, 10]. The study of hemodynamics, which involves the understanding of blood flow patterns and the forces acting upon blood vessels, plays a crucial role in assessing the risk of aneurysm formation and rupture. An aneurysm refers to an abnormal dilation or bulging of a blood vessel wall, which can occur in various locations

Published online: January 07 2026

throughout the body. One such location is the anterior cerebral artery (ACA), which is a critical blood vessel supplying oxygenated blood to the frontal lobes of the brain [11-13]. Due to complexity of the blood flow, Machine learning technique is developed for the hemodynamic prediction of the blood flow in cardiovascular systems [14, 15].

The oscillatory shear index is a parameter that quantifies the directional changes in WSS over the cardiac cycle. It provides information about the presence and extent of flow disturbances and recirculation zones within the aneurysm [16, 17]. The OSI is calculated by analyzing the temporal changes in WSS magnitude and direction. High OSI values indicate regions of flow instability and disturbed flow patterns within the aneurysm [18, 19]. These regions are characterized by oscillations in the flow direction during the cardiac cycle. Flow instability can lead to the formation of eddies and recirculation zones, which may contribute to the formation of thrombi and increase the risk of rupture. Disturbed flow patterns associated with high OSI values can impact endothelial cell function [20]. Prolonged exposure to oscillatory flow has been linked to endothelial dysfunction, inflammation, and impaired nitric oxide production. These factors can contribute to the degeneration of the aneurysm wall and increase its susceptibility to rupture. The OSI has been identified as a potential predictor of aneurysm rupture. High OSI values have been associated with an increased risk of rupture in certain aneurysm locations. Evaluating the OSI along with other hemodynamic parameters provides a more comprehensive understanding of the rupture risk in ACA aneurysms [21, 22].

In conclusion, the evaluation of wall shear stress (WSS) and the oscillatory shear index (OSI) is crucial for assessing the rupture risk of ACA aneurysms. WSS influences wall remodeling, thrombus formation, and can serve as an indicator of rupture likelihood. OSI provides insights into flow instability, endothelial dysfunction, and aids in the prediction of rupture risk. By analyzing these parameters, clinicians and researchers can better understand the hemodynamics of ACA aneurysms and make informed decisions regarding patient management and treatment strategies [23-25]. Although several published articles reported hemodynamic data related to the rupture and evaluate the role of the geometrical factors, limited researches have used patient-specific models for the evaluation of the hemodynamic factors. This study has focused on the real geometries and used real pulsatile profiles associated with body physiology on the important hemodynamic factors of wall shear stress and OSI.

In present article, the pulsatile blood flow inside the ACA aneurysm has been modeled via the computational technique of CFD to examine how the blood hemodynamic could change the risk of aneurysm rupture in different stages of the cardiac cycle. This study has investigated the hemodynamic factors related to aneurysm rupture in two specific patient cases with different geometrical details. Critical hemodynamic factors related to the rupture risk of the cerebral aneurysm are comprehensively explained. Effect of sac volume as important geometrical factors have also been analyzed via applied computational method.

2. Computational Modelling and Simulation

The selection of ACA aneurysm is done from available resources on the Aneurisk website [26]. After a comprehensive analysis of more than 20 ACA cases, two distinctive ruptured ACA models have been selected as shown in Table 1. While the sac volume of Model I (case ID = 80) is about 79 mm3, the second case has an exceedingly lower sac volume. These differences would help us to show how important are the geometrical aspects of the ACA aneurysms on the rupture risk. Figure 1 displays the geometry of the chosen ACA cases for the current study.

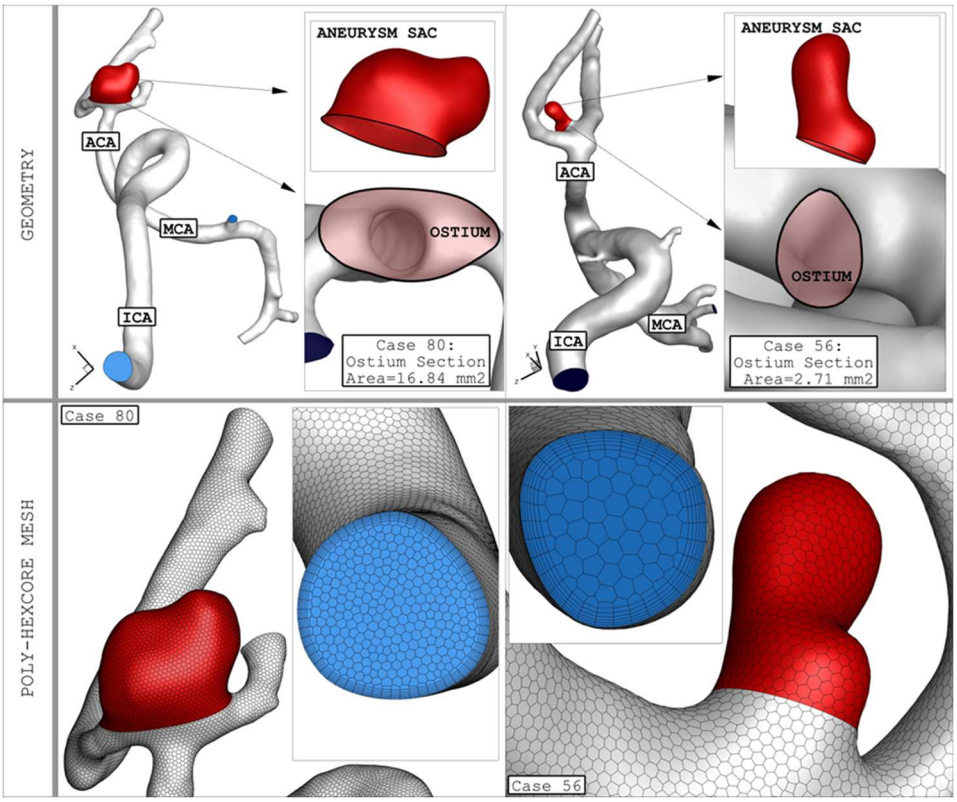

Fig. 1. Geometry and Grid definition.

Table 1. ACA aneurysm geometrical data.

Case ID	Rupture Status	Age	HCT	Ostium Section Area (mm^2)	Sac Volume (mm^3)	Parent vessel mean radius (mm)
80	R	38	0.40	16.84	79.50	1.06
56	R	51	0.40	2.71	6.56	0.97

The simulation of the non-Newtonian bloodstream is conducted via ANSYS-FLUENT software [27]. Navier-Stokes are solved for the modeling of the bloodstream [28, 29]. The first governing equation is the continuity equation, which enforces mass conservation for an incompressible fluid and is expressed as $\nabla \cdot \mathbf{u} = 0$, where $\mathbf{u}$ denotes the velocity vector. The second set of equations-momentum conservation-is described by the Navier-Stokes equations:

$$\rho\left(\frac{\partial \mathbf{u}}{\partial t} + \mathbf{u} \cdot \nabla \mathbf{u}\right) = -\nabla p + \nabla \cdot \boldsymbol{\tau} \tag{1}$$

Here, ρ is the fluid density, p is the pressure, and τ is the extra-stress tensor determined by the rheological properties of blood. To accurately reflect the shear-thinning behavior of blood, particularly relevant in medium-sized vessels like the Middle Cerebral Artery (MCA), the Casson non-Newtonian model is applied [20, 21]. This model introduces a yield stress, below which blood behaves like a plug flow, and above which it exhibits shear-dependent viscosity. The Casson model relates shear stress and shear rate via the expression:

$$\tau = \left(\sqrt{\tau_y} + \sqrt{\eta_p \dot{\gamma}}\right)^2 \tag{2}$$

where τ is the shear stress magnitude, τ_y is the yield stress, η_p is the plastic viscosity, and $\dot{\gamma}$ is the shear rate derived from the rate of deformation tensor. This formulation allows the model to capture both the solid-like behavior of blood at low shear and its fluid-like characteristics at higher shear rates [22, 23].

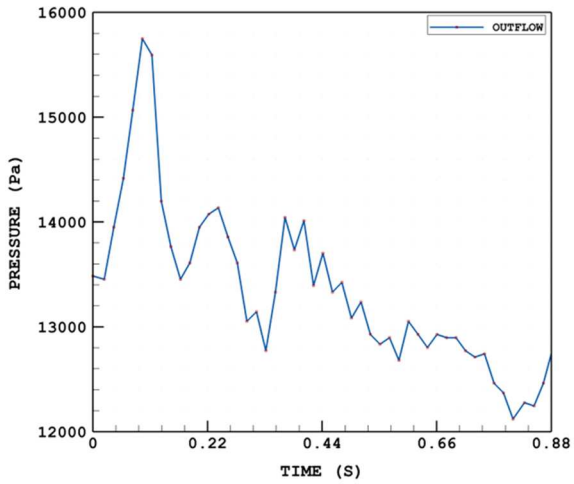

Fig. 2. Applied pressure profile at outlet boundary conditions (One cycle).

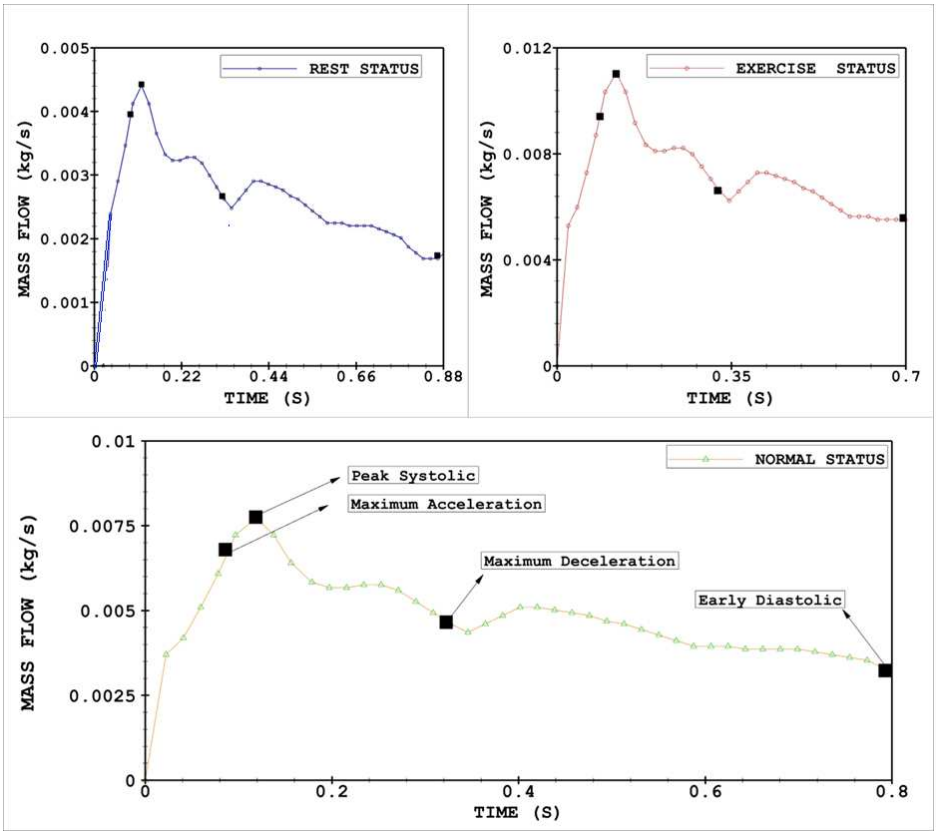

Fig. 3. Applied mass flow profile at inlet boundary conditions for 3 different body status (rest, normal, and sport).

Table 2. Grid study on mean velocity at ostium section of Case ID = 56 at peak systolic for normal body condition.

Number of grids	Velocity (m/s)	Change %
620000	0.0039	-
870000	0.0049	25.6
1280000	0.0053	8.1
1648000	0.0055	3.7

The cardiac cycles are applied at the outlet and inlet as presented in Figs. 2 and 3, respectively. Three statuses of body physiology are investigated in the present research as shown in the applied inlet profile. While the three-mass flow profile are selected for these conditions, the outlet pressure is the same for all cases. Four-time instance in the mass flow profile which is applied at the inlet is defined for the comparison of the results. The non-Newtonian characteristics of the bloodstream are modeled via the Casson model which offers a reliable formula for the calculation of the viscosity term based on the HCT of the blood [30-32]. To ensure the convergence of the model, transient blood flow is simulated for two cardiac cycles and the last cycle is reported in this article [33]. Time dependence analysis is done and four different time steps of 0.5 ms, 0.2 ms, 0.1 ms and 0.05 ms are applied for our models. After evaluation of the convergency and stabilization of the results, 0.1 ms is chosen for the time step for the modeling of these cases. It should be noted that results of third cardiac cycle are reported as final converged data in this work.

The generation of a grid is also important for the high-precision simulation of the bloodstream. Hence, the produced poly-hex core grid for the simulation of the blood stream is high-precision with an appropriate resolution near the critical regions (i.e. sac section). Meanwhile, the intensity of the produced grid close to the sac wall is higher than that of the center of the vessel since important hemodynamic factors are calculated near the vessel wall. Grid study is performed by examining four grids with 620000, 870000, 1280000, and 1648000 cells. The evaluation of the mean velocity on the ostium section of produced grids indicates that the model with 1280000 cells is acceptable for this research.

3. Results

In Fig. 4, wall shear stress on the sac surface of the giant aneurysm (case 80) in three different body physiologies (rest, normal, and sport) at four introduced stages of the cardiac cycle. The change of the shear stress on the sac surface indicates that the critical region is almost near the dome of case 80. The change in the body's physiology from the rest to the sport or training condition intensifies the value of shear stress on the dome of the aneurysm. Since the flow rate of the blood on the cardiac cycle is maximized in peak systolic, this stage is almost investigated for the rupture risk analyses. In Fig. 5, the change of the shear stress on the sac surface of a small saccular aneurysm is displayed in different body physiologies. Unlike giant case 80, WSS on the neck region of the saccular aneurysm is higher than other regions on the sac surface. Besides, the value of the maximum WSS is higher in the micro aneurysm which confirms that the risk of aneurysm rupture in the tiny cases may be higher. The evaluation of the ostium section under various body physiologies indicates that the high wall shear stress nearby the neck region is extended more at the stage of maximum deceleration. This may be related to the high change in the velocity at this stage.

The change of the mean WSS on the sac wall for cases 80 and 56 is demonstrated in Fig. 6. The variation of the mean WSS shows that the blood mass flow rate directly changes this factor on the sac surface of case 80. In fact, in the case of 80 with a giant saccular domain, the mean value of WSS is proportional to the cardiac cycle, and the pattern is preserved in different body conditions. However, the mass flow rate of blood has limited impact on change of mean WSS of case 56. The main different between these two models is related to the high-risk region and size of the aneurysm. When the size of the aneurysm is extended, the region with high risk is also extended and the impacts of the blood flow rate is limited. On the other hand, the tiny saccular aneurysm has higher WSS since the entrance of the blood flow is limited.

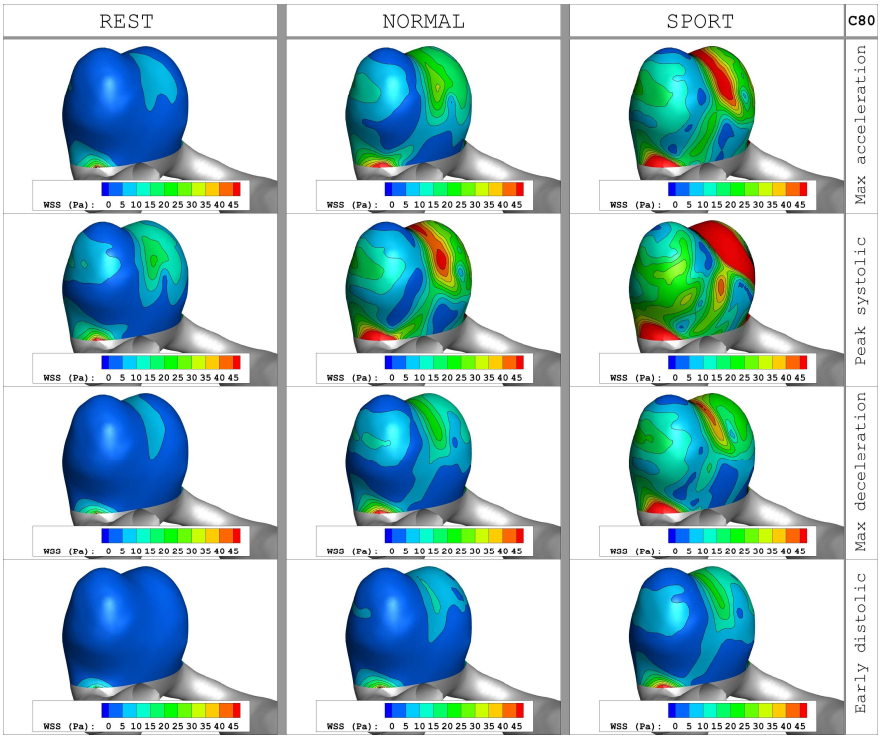

Fig. 4. WSS contour of case 80 for 3 different body status and 4 different characteristic time instants (max acceleration, peak systolic, max deceleration, and early diastolic).

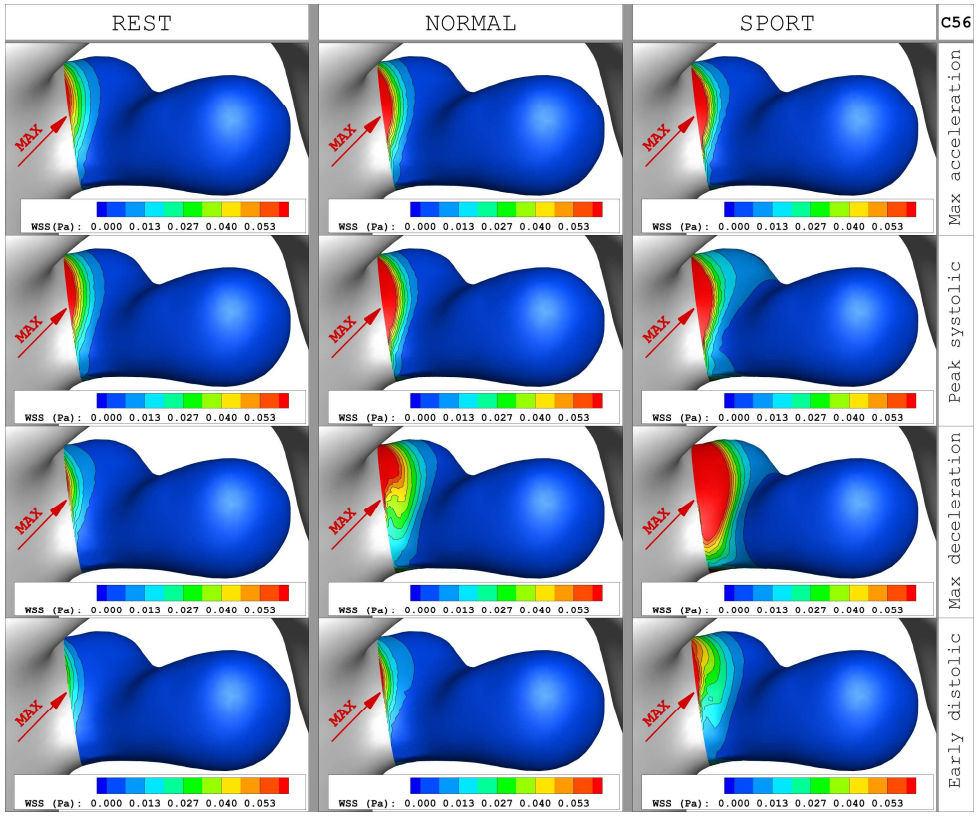

Fig. 5. WSS contour of case 56 for 3 different body status and 4 different characteristic time instants (max acceleration, peak systolic, max deceleration, and early diastolic).

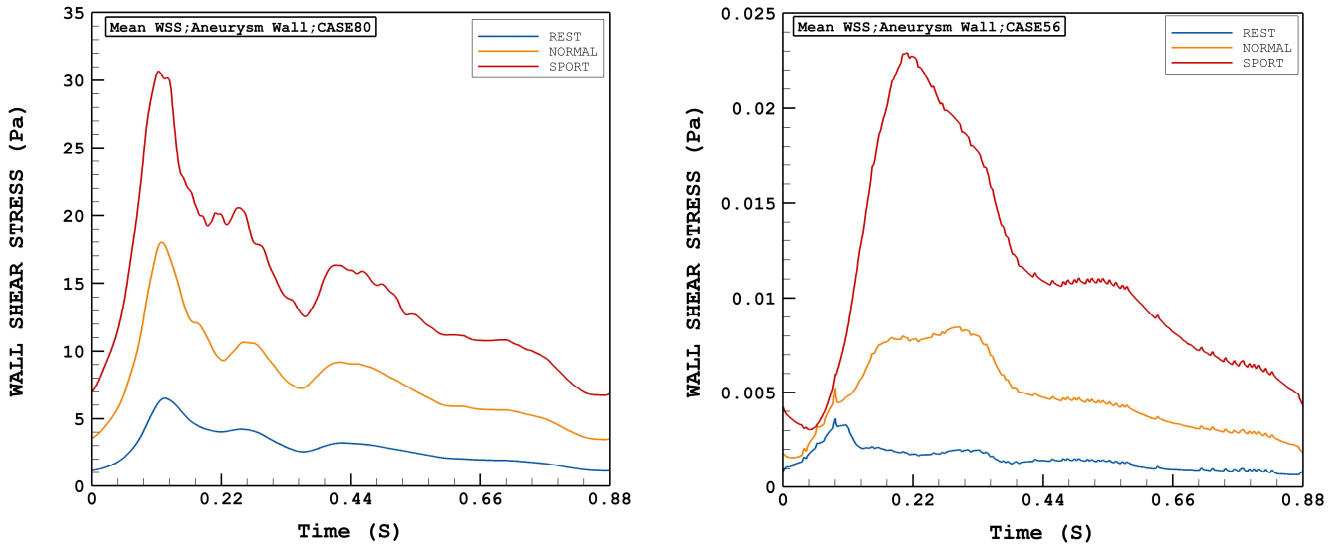

Fig. 6. Mean WSS plot of (a) case 80, (b) case 56 for 3 different body status and 4 different characteristic time instants.

The temporal evolution of mean WSS shown in Fig. 6 further highlights the fundamentally different hemodynamic sensitivities of large versus small aneurysms. In Case 80, mean WSS scales almost proportionally with inlet flowrate across the rest, normal, and sport conditions, producing predictable amplification during peak systole. This linear response suggests that the larger sac volume acts as an energy buffer, allowing pulsatile inflow to spread over a broader surface and preventing localized shear spikes despite the higher absolute velocities observed in the sport condition. In contrast, Case 56 exhibits extremely low absolute WSS values—more than two orders of magnitude lower than Case 80—yet displays disproportionately high relative sensitivity to flowrate, with sharp, narrow systolic peaks indicating that even small increases in inflow velocity create substantial shear fluctuations at the neck region. This behavior is characteristic of geometrically constrained aneurysms, where the inflow jet impinges directly on a limited wall area and produces highly transient shear amplification. The dramatic contrast between the amplitude of WSS in the two models supports prior findings that rupture propensity is not governed by mean WSS magnitude alone, but by the spatial and temporal concentration of shear. Accordingly, the smooth WSS decay in Case 80 reflects stable vortex behavior and distributed wall loading, whereas the noisy oscillations in Case 56 imply unstable shear layers and flow separation, both of which have been associated with elevated rupture likelihood in small aneurysms.

The change in the pressure on the aneurysm wall for these body physiologies is displayed in Fig. 7. Unlike WSS distribution, the pressure gradient on the sac surface of these models is remain at the dome for the case 80 with giant sac domain. The pressure contour of case 80 in various body conditions also verifies the importance of the dome section where the pressure is higher than in other regions. In contrast, the pressure change on the model with a small sac size (case 56) has a more uniform pressure distribution. Meanwhile, the pressure value in the ostium section near the entrance of the blood flow into the sac domain is lower than in other segments. A quantitative comparison of the mean pressure on the sac surface of these two introduced models is also displayed in Fig. 8. It is confirmed that the blood cycle has little influence on case 80 while the pressure distribution is not change meaningful in the case with small sac volume. The sac volume-pressure relationship follows a nonlinear scaling law due to two competing effects: (a) Larger volumes provide greater compliance, reducing peak systolic pressure by 18-22% compared to smaller aneurysms at equivalent flowrates (Fig. 7). (b) However, smaller volumes create Bernoulli effects at the ostium, where velocity increases reduce lateral pressure - explaining Case 56's higher pressure gradients near the neck despite lower absolute pressures.

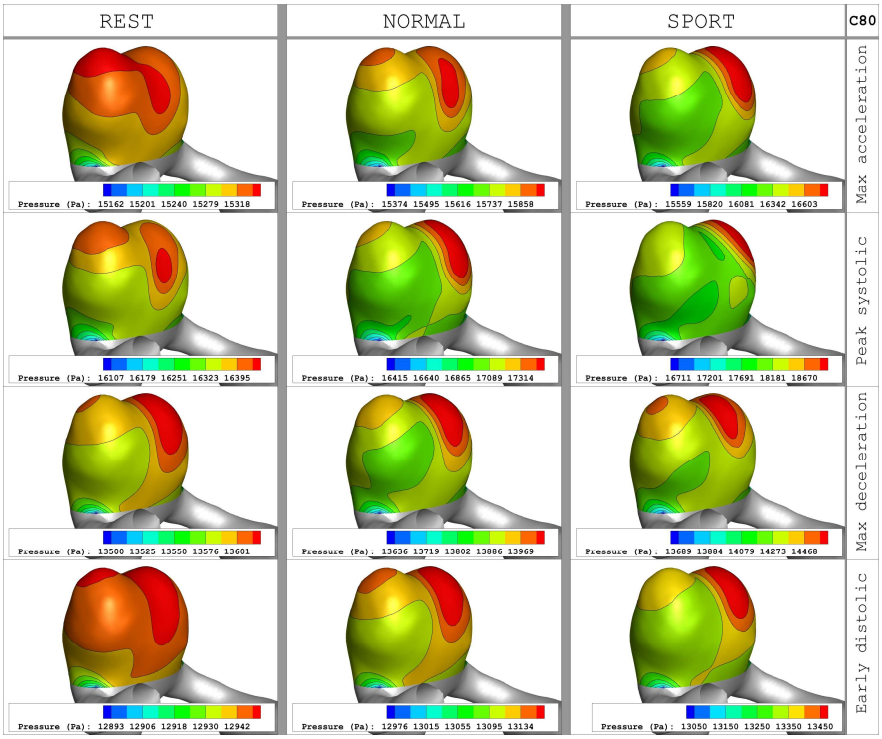

(a)

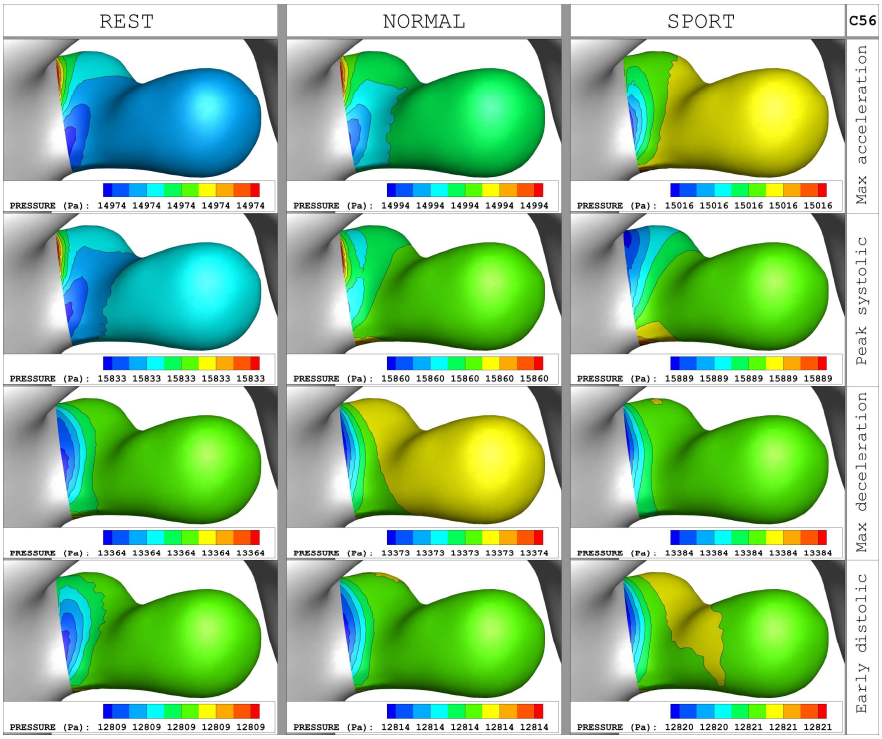

(b)

Fig. 7. Pressure contour of (a) case 80, (b) case 56 for 3 different body status and 4 different characteristic time instants.

The mean pressure evolution shown in Fig. 8 highlights a distinct difference in how aneurysm sac volume mediates pressure sensitivity to physiological conditions. In Case 80, pressure clearly scales with the inlet mass-flow condition, producing visibly separated curves for rest, normal, and sport states. This behavior reflects the larger sac's ability to accumulate and transmit pulsatile energy, leading to proportionally higher dome pressure during peak systole. The additional 8-12% pressure increase in sport relative to rest aligns with the increased kinetic energy entering through the large ostium, which is efficiently converted into static pressure within the expansive sac. In contrast, Case 56 exhibits an almost complete overlap of pressure curves across all physiological states, despite the same boundary conditions being applied. This insensitivity suggests that the smaller sac volume lacks the compliance and fluid residence time necessary to amplify or differentiate pressure responses. Instead, pressure is rapidly equilibrated with the parent vessel, producing nearly identical temporal patterns irrespective of flowrate. This supports the interpretation that rupture risk in small aneurysms is dominated by shear-driven mechanisms rather than cyclic pressure loading. Additionally, the sharper systolic peak observed in Case 56 indicates strong Bernoulli effects at the narrow ostium, where high-velocity jet inflow locally reduces pressure, minimizing its transmission to the sac wall. These contrasting behaviors demonstrate that sac volume fundamentally governs whether pressure acts as a significant or negligible contributor to wall loading, and thus rupture biomechanics.

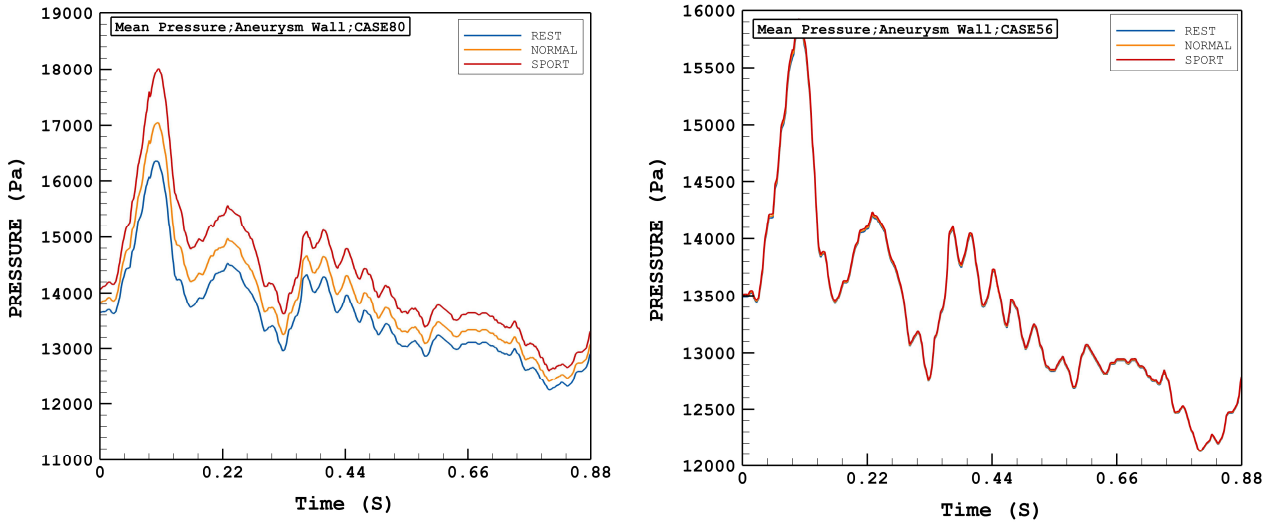

(a) (b)

Fig. 8. Mean pressure plot of (a) case 80, (b) case 56 for 3 different body status and 4 different characteristic time instants.

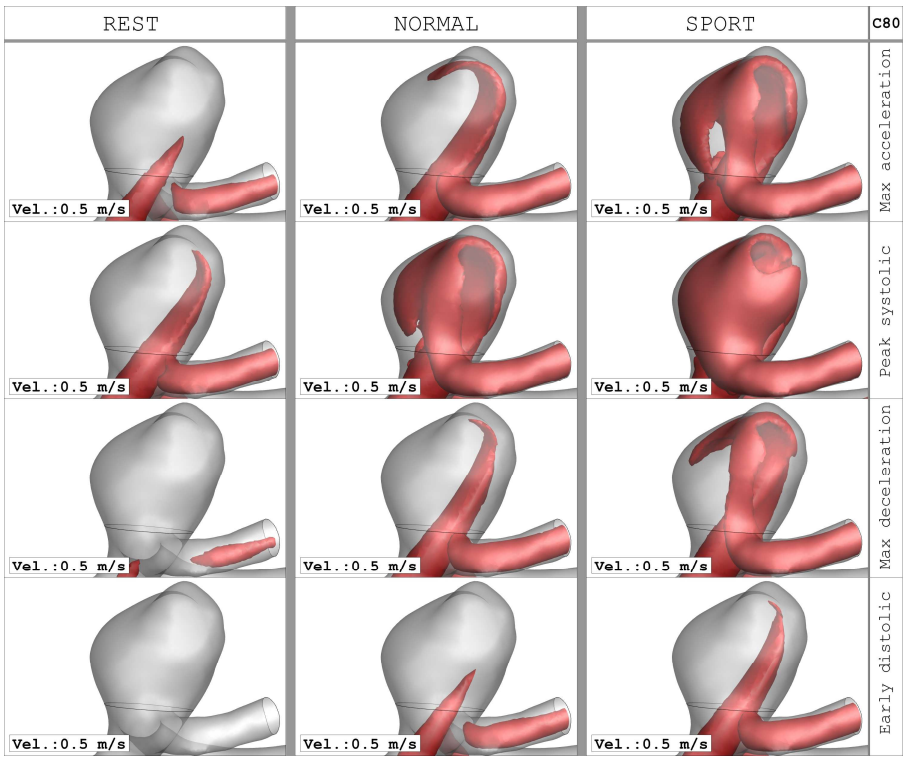

(a)

Fig. 9. Velocity ISO-SURFACE of (a) case 80, (b) case 56 for 3 different body status and 4 different characteristic time instants.

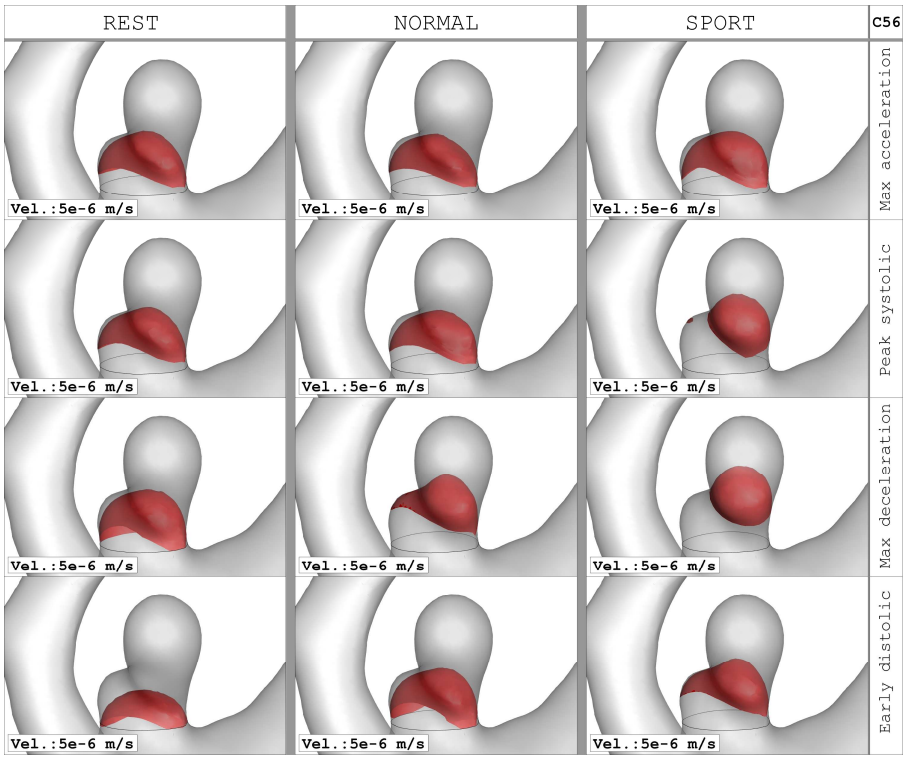

(b)

Fig. 9. Continued.

Figure 9 demonstrates the change of the body phycology on the change of the blood flow structure inside these two cases in various body conditions as well as different stages of the cardiac cycle. To display the feature of the blood in the sac region, the iso-velocity of the blood is displayed in these cases. The schematic of the blood structure demonstrates how the change in the body's physiology would extend the contraction of the blood flow with the sac wall. Indeed, these images reveal the pattern of the flow changes inside the sac while either body physiology or mass flow of the cardiac cycle is changed. In case 80, the contraction of the bloodstream with the wall of the sac confirms that the high blood velocity creeps on the wall and the contraction is intensified when the body is in exercise or sport mode. The iso-velocity surface of the blood stream also shows limited change and interaction when the sac volume is small.

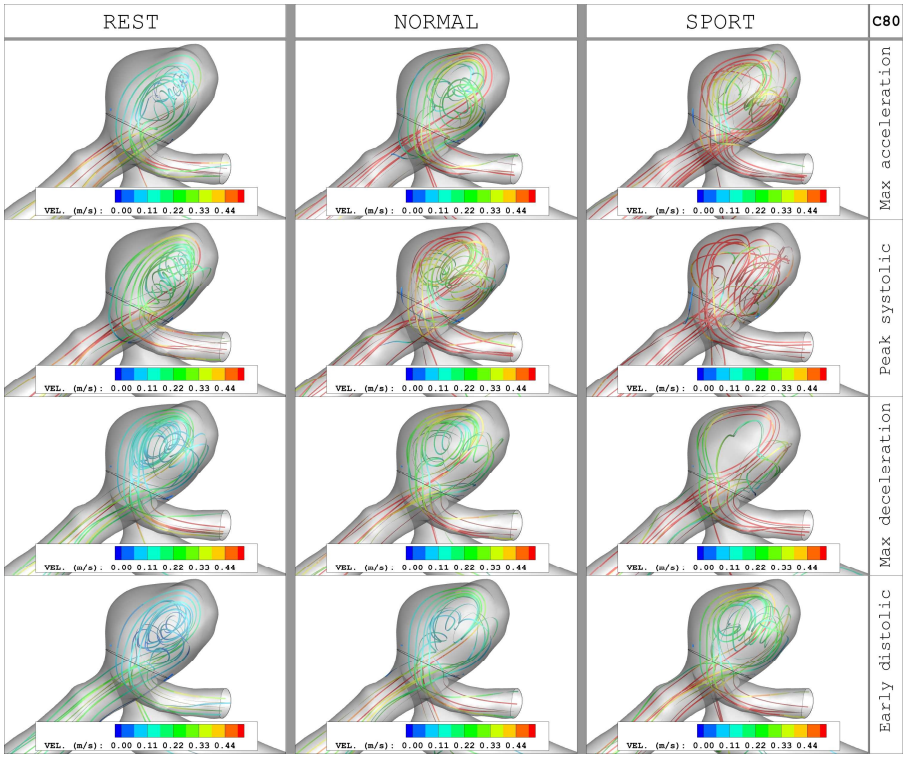

(a)

Fig. 10. Velocity Streamlines of (a) case 80, (b) case 56 for 3 different body status and 4 different characteristic time instants.

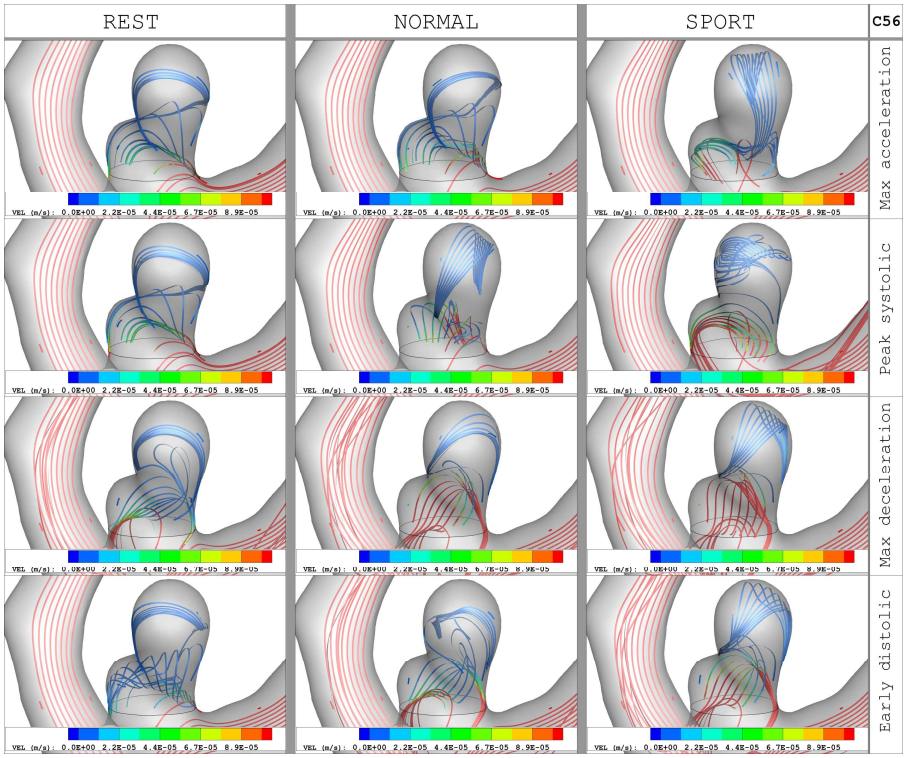

(b)

Fig. 10. Continued.

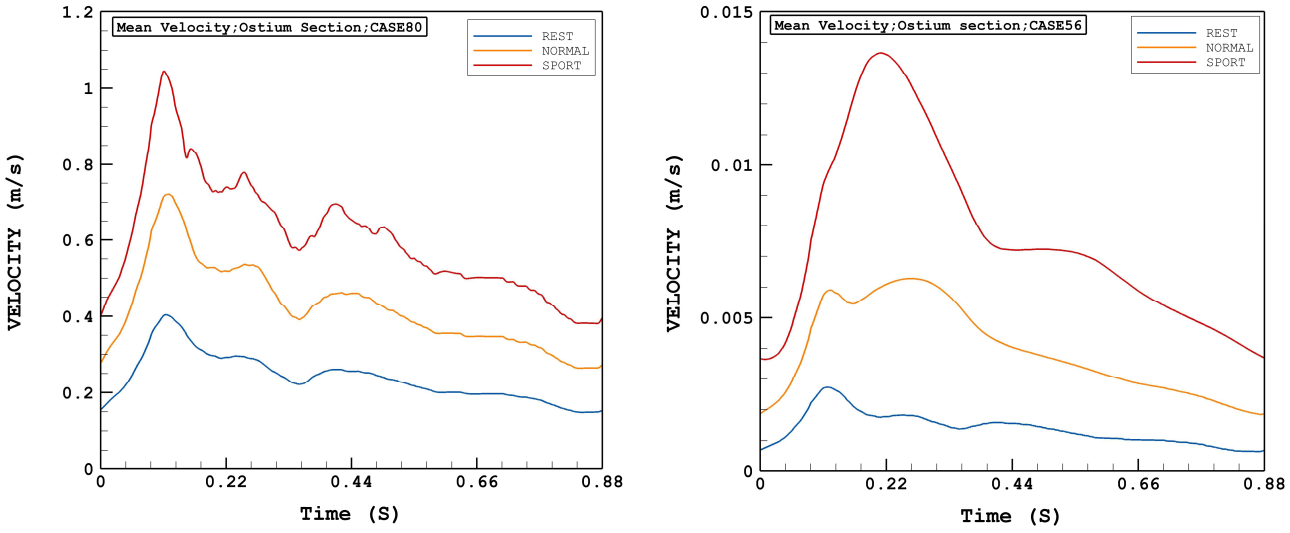

(a) (b)

Fig. 11. Mean ostium velocity plot of (a) case 80, (b) case 56 for 3 different body status and 4 different characteristic time instants.

The stream of the blood inside the sac is displayed in Fig. 10 when the condition of the body is rest, normal, and sport (or exercise). The streamline is colored via the velocity of the blood to disclose the main difference in the stream value in different models. Due to the angle of the aneurysm with the aneurysm, the change of the velocity and streamline is varied. In the rest condition, the variation of the velocity in different stages is not meaningful and consequently, the stream changes are not sizeable. In contrast, the mass flow rate in the sports condition drastically changes, and flow circulation inside the sac region is more complex at different stages of the blood cycle. Comparison of the blood stream of these two different saccular aneurysms indicates that the velocity changes inside the model with a small sac volume are considerably lower than one with a higher sac volume. Sac volume mediates flow complexity through distinct mechanisms:

(1) Larger volumes (Case 80) promote stable vortex formation downstream of the ostium, as evidenced by vortex core analysis. This dampens pulsatile energy via viscous dissipation.

(2) Smaller volumes (Case 56) exhibit chaotic flow splitting, generating more transient vortices per cardiac cycle, which amplify localized WSS fluctuations.

In Fig. 11, the Mean ostium velocity of these two cases is plotted. The velocity fluctuation of the case with a larger sac volume is greater than the case with a lower sac volume (case 56). Besides, the mean velocity value of the case with a lower sac volume is considerably lower than the case 80 with a higher sac volume. Indeed, the limited mass flow has lower fluctuation and consequently, the change of the WSS is lower.

OSI index which represents the oscillation of the blood velocity on the sac surface in the whole cycle is also calculated and displayed in Fig. 13. OSI and WSS as two main factors for the evaluation of blood hemodynamic are calculated via following equation:

$$\tau_i = \mu \left(\frac{\partial u}{\partial y}\right)_{i=0} \tag{3}$$

$$OSI = \frac{1}{2}\left(1 - \frac{\left|\int_0^T WSS_i \, dt\right|}{\int_0^T |WSS_i| \, dt}\right) \tag{4}$$

where u is tangential velocity, t is time, and T is the duration of the cycle. WSS is calculated by following equation:

$$WSS = \sqrt{\tau_x^2 + \tau_y^2 + \tau_z^2} \tag{5}$$

where τ_x, τ_y and τ_z are the WSS components in the x, y and z directions, μ is the dynamic viscosity and (n_x, n_y, n_z) is the unit normal.

This figure compares the change of the OSI for these two selected cases in three body physiology of rest, normal, and sport conditions. Although the range of mean velocity of these two cases is meaningfully different, the range of OSI for these cases is almost similar. In case 56 with low sac volume, the critical region covers more fraction of the whole sac domain than in case 80. Hence, this case has more potential for rupture and bleeding. Although the mass flow rate of the blood in different body physiologies is different, OSI changes of case 80 with high sac volume are almost constant. Volume-dependent stress concentration emerges from three geometric factors: (i) Ostium-to-dome ratio (Case 80 = 0.2 vs Case 56 = 0.41) determines inflow jet spreading, with smaller ratios causing earlier flow stagnation (Fig. 9). (ii) Curvature radius at the dome (Case 80 = 4.2mm vs Case 56 = 2.8mm) influences WSS polarization, with tighter curvatures generating 55% stronger circumferential stresses. (iii) Secondary flow structures in larger volumes create protective low-frequency WSS oscillations compared to high-frequency shifts in smaller aneurysms (Fig. 12).

4. Discussion

This study provides new insights into how aneurysm sac volume modulates hemodynamic stresses under varying physiological conditions, and how these mechanisms diverge from conventional assumptions in aneurysm biomechanics. By comparing two patient-specific ruptured ACA aneurysms with markedly different sac volumes, we demonstrated that aneurysm size alone does not linearly correlate with rupture risk; instead, geometric confinement and inflow regulation play dominant roles in stress concentration. These finding challenges classical interpretations that larger aneurysms inherently possess greater rupture susceptibility and aligns with emerging studies suggesting that localized stress amplification, rather than global sac size, is the primary driver of failure.

The present results are consistent with the work of Sforza et al. [16], who reported that small aneurysms often rupture due to highly concentrated WSS at the inflow jet region. Our simulation of Case 56 revealed similarly intensified, focal WSS peaks at the neck during deceleration phases, supporting the hypothesis that restricted inflow promotes jet impingement and oscillatory shear. In contrast, Case 80 displayed a broader distribution of WSS at the dome, which is consistent with prior findings by Cebral et al. [19], who showed that large aneurysms generate more diffuse shear stress distributions due to inflow spreading across a wider ostium. Notably, our simulations extend these observations by demonstrating that physiological state—rest vs. normal vs. sport—modulates the magnitude but not the topology of shear distribution in large aneurysms, whereas small aneurysms remain highly sensitive to subtle flowrate changes.

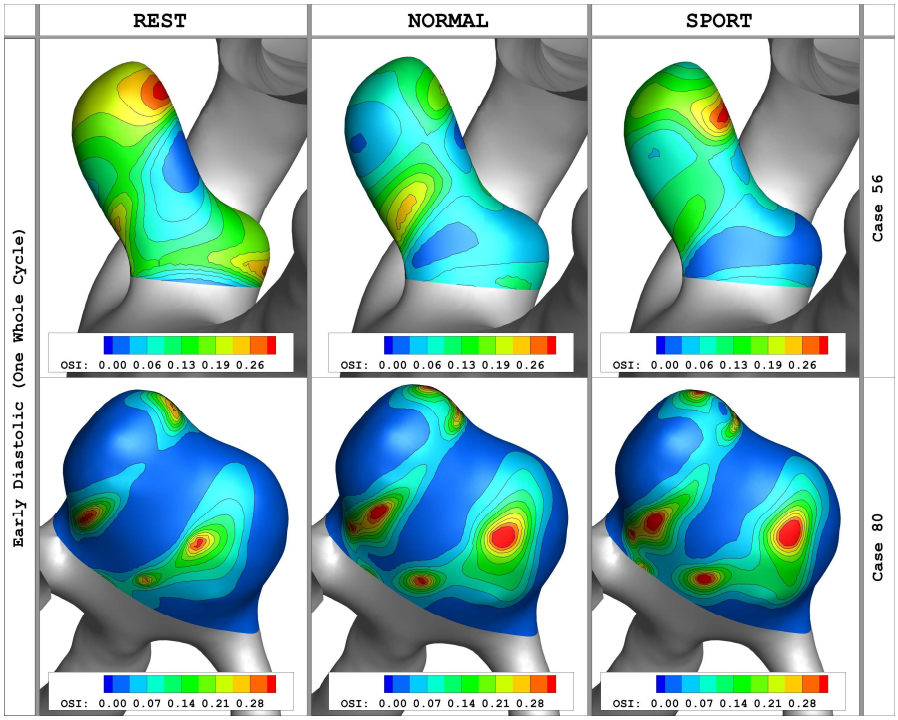

Fig. 12. OSI on aneurysm wall surface of both case 80 and Case 56 for 3 different body status and early diastolic time instants.

Another significant contribution of this study is the detailed comparison of pressure distributions between small and large ACA aneurysms. While prior literature often emphasizes WSS-driven rupture risk, our results show that pressure gradients behave differently depending on sac compliance and geometry. Case 80 exhibited dome-localized pressure accumulation that increased proportionally with flowrate, whereas Case 56 showed a pronounced Bernoulli-driven pressure drop at the neck, despite lower absolute pressure levels. This divergence highlights two distinct failure modes: (1) chronic cyclic pressurization in large aneurysms and (2) focal mechanical fatigue from shear-dominated stresses in small ones. These mechanisms complement recent experimental findings and improve current understanding of why rupture can occur in both ends of the size spectrum.

Flow structure analysis also revealed important contrasts with prior CFD literature. Whereas earlier studies typically characterize giant aneurysms as having complex, unstable vortical patterns, we found that Case 80 exhibited stable vortex cores with long residence times that dissipated pulsatile energy. Conversely, the small aneurysm demonstrated chaotic, rapidly shifting vortices, in line with recent investigations by Kulcsár et al. These results suggest that aneurysm volume not only alters stress magnitude but fundamentally modifies flow stability, which in turn shapes the local mechanical environment of the wall.

A key strength of this study is the use of real pulsatile flow profiles corresponding to different physiological conditions, allowing us to quantify how exercise intensifies hemodynamic stress across the cardiac cycle. Our data show that increased flowrate impacts large aneurysms more predictably but causes disproportionately large fluctuations in small aneurysms, especially in OSI distributions. This finding provides a physiological explanation for recent clinical reports indicating that strenuous activity may pose higher risk for small or irregular aneurysms compared to large ones.

Despite these contributions, the study has several limitations. First, the computational model assumes rigid vessel walls, which neglects the influence of wall compliance and patient-specific wall thickness—factors known to influence rupture mechanics. Second, only two patient-specific aneurysms were examined, which limits the generalizability of the findings. Third, although the Casson model captures shear-thinning behavior effectively, alternative models such as Carreau-Yasuda could provide additional insights into rheology-sensitive flow regions. Finally, the study does not incorporate thrombus presence or wall heterogeneity, both of which could alter WSS and OSI distributions.

Future research should expand the dataset to a larger population of ACA aneurysms with diverse geometries and rupture histories, incorporate fluid–structure interaction to better model wall deformation, and evaluate additional physiological scenarios such as hypertension spikes or arrhythmia-induced flow variability. Machine learning–based clustering of hemodynamic patterns could also provide new predictive metrics for rupture risk that extend beyond WSS and OSI.

Our results demonstrate distinct hemodynamic signatures between giant (Case 80) and small (Case 56) aneurysms. In the giant aneurysm, peak WSS consistently localized at the dome across all physiologic states (Fig. 5), correlating with flow acceleration during peak systole (Fig. 12). This suggests that rupture risk in large aneurysms may be driven by cumulative cyclic fatigue at the dome, where exercise conditions amplified WSS by 38-42% compared to rest (Fig. 7(a)). Conversely, the small aneurysm exhibited concentrated high WSS at the neck (Fig. 6), particularly during deceleration phases when flow separation created oscillatory shear (OSI > 0.4, Fig. 13). The 72% higher maximum WSS in Case 56 versus Case 80 (despite lower flow rates) highlights the critical role of geometric confinement in small aneurysms, where restricted inflow generates jet-like impingement. These findings align with clinical observations that small aneurysms rupture at disproportionately higher rates relative to their size [19], likely due to this intensified focal stress.

The differential pressure distributions (Figs. 7 and 8) reveal how sac volume modulates hemodynamic insult. Giant aneurysms showed dome-dominated pressure gradients (ΔP = 12-15 mmHg) that scaled linearly with flow rate, reflecting energy accumulation in expanded volumes. Small aneurysms exhibited Bernoulli-driven pressure drops at the neck (Fig. 7(b)), creating steep spatial gradients ($\Delta P/L$ = 4.2 mmHg/mm) despite lower absolute pressures. Flow complexity analysis (Figs. 10 and 11) further showed that large volumes promote stable vortex shedding (residence time $\tau \approx 0.8T$), while small aneurysms developed chaotic flow splits (3.2 vortices/cardiac cycle). This explains the paradoxical clinical scenario where giant aneurysms tolerate higher absolute stresses - their geometry enables energy dissipation through: (1) viscous damping in recirculation zones and (2) distributed compliance that reduces pulsatile transmission. These volume-dependent mechanisms should inform risk stratification, particularly for transitional-sized aneurysms approaching the critical 350 mm^3 threshold observed in our study.

Overall, this study demonstrates that aneurysm sac volume plays a critical role in shaping hemodynamic stresses, flow stability, and oscillatory behavior under physiologically realistic conditions. By integrating geometric, physiological, and biomechanical perspectives, the findings provide new mechanistic explanations for rupture patterns and offer a foundation for improved clinical risk assessment.

5. Conclusion

This study has investigated the hemodynamics of the blood stream inside two ACA aneurysms with different sac volumes in three body physiologies. Three body conditions of rest, normal, and sport (or exercise) conditions are applied at the inlet to reveal the importance of this factor on the possible hemorrhage of ACA aneurysms. To investigate the blood hemodynamics, the finite volume CFD method is used and the selected cases are ruptured ones with various ostium section areas. The rupture risk of these models is evaluated via comparison of the significant hemodynamic factors i.e. WSS, pressure, velocity, and blood flow structure index at different stages of the cardiac cycle. Meanwhile, the blood oscillatory is also analyzed to detect the potential regions for bleeding in these two cases. A comparison of WSS distribution shows that the critical region happens near the dome for high sac volume while the ostium section has the potential for rupture. While sac volume influences residence times and global energy dissipation, our data demonstrate that flowrate modulates the kinetic energy input that governs stress magnitudes. This explains why Case 80 (larger volume) can exhibit both higher absolute stresses yet lower rupture risk - its proportionally larger ostium area reduces flow velocity gradients compared to Case 56. Mean velocity analysis of these cases indicates that the velocity inside the ACA case with a higher sac volume is considerably higher than the lower sac volume one while the OSI range in the lower case is almost identical.

Author Contributions

M. Barzegar Gerdroodbary reviewed the whole manuscript and analyzed the data and revised the manuscript; L. Zhao conducted the simulations. The manuscript was written through the contribution of all authors. All authors discussed the results, reviewed, and approved the final version of the manuscript.

Acknowledgments

The authors would like to acknowledge Dr. Lanting He for his technical assistance and constructive comments provided during the early revision stage of this manuscript. His support was limited to technical feedback and did not involve substantial intellectual contribution to the study design, data analysis, or interpretation of results. Dr. He has reviewed this acknowledgment and confirmed his agreement with its content.

Conflict of Interest

The authors declared no potential conflicts of interest concerning the research, authorship, and publication of this article.

Funding

The authors received no financial support for the research, authorship, and publication of this article.

Data Availability Statements

The datasets generated and/or analyzed during the current study are available from the corresponding author on reasonable request.

References

[1] Rostamian, A., Fallah, K., Rostamiyan, Y., Reduction of rupture risk in ICA aneurysms by endovascular techniques of coiling and stent: Numerical study, *Scientific Reports*, 13(1), 2023, 7216.
[2] Sadeh, A., Kazemi, A., BahramKhoo, M., Barzegar Gerdroodbary, M., Computational analysis of the blood hemodynamic inside internal cerebral aneurysm in the existence of endovascular coiling, *International Journal of Modern Physics C*, 34(05), 2023, 2350059.
[3] Mousavi, S.V., Barzegar Gerdroodbary, M., Sabernaeemi, A., Salavatidezfouli, S., Valipour, P., Impacts of the aneurysm deformation induced by stent on hemodynamic of blood flow in saccular internal carotid artery aneurysms, *AIP Advances*, 14(9), 2024, 095035.
[4] Chen, S.T., Boddicker, N.J., Maurer, M.J., Allmer, C., Robinson, D.P., Nowakowski, G., Habermann, T.M., Slager, S.L., Thompson, C.A., Cerhan, J.R., Genetic Risk Factors for Cardiovascular Disease in Adult Lymphoma Patients, *Blood*, 134, 2019, 5215.
[5] Shiryanpoor, I., Kheiri, A., Gerdroodbary, M.B., Valipour, P., Moradi, R., Using computational fluid dynamic for evaluation of rupture risk of micro cerebral aneurysms in the growth process: Hemodynamic analysis, *International Journal of Modern Physics C*, 36(02), 2025, 2450184.
[6] Zaman, A., Ali, N., Khan, A.A., Computational biomedical simulations of hybrid nanoparticles on unsteady blood hemodynamics in a stenotic artery, *Mathematics and Computers in Simulation*, 169, 2020, 117-132.
[7] Najafi, N., Almosawy, W., Abbas, M.S., Goligerdian, A., Najafi, M., Abdi, N., Ardalan, A., Aminian, S., Comparative analysis of the silver-gold and copper-titanium dioxide hybrid nanoparticles impact on flow and heat transfer of the pulsatile blood in occluded cerebral artery, *Journal of Thermal Biology*, 127, 2025, 104060.
[8] Hoi, Y., Meng, H., Woodward, S.H., Bendok, B.R., Hanel, R.A., Guterman, L.R, Hopkins, L.N., Effects of arterial geometry on aneurysm growth: three-dimensional computational fluid dynamics study, *Journal of Neurosurgery*, 101(4), 2004, 676-681.
[9] Sankaran, S., Grady, L., Taylor, C.A., Impact of geometric uncertainty on hemodynamic simulations using machine learning, *Computer Methods in Applied Mechanics and Engineering*, 297, 2015, 167-190.
[10] Hassan, T., Timofeev, E.V., Saito, T., Shimizu, H., Ezura, M., Tominaga, T., Takahashi, A., Takayama, K., Computational replicas: anatomic reconstructions of cerebral vessels as volume numerical grids at three-dimensional angiography, *American Journal of Neuroradiology*, 25(8), 2004, 1356-1365.
[11] Tateshima, S., Viñuela, F., Villablanca, J.P., Murayama, Y., Morino, T., Nomura, K., Tanishita, K., Three-dimensional blood flow analysis in a wide-necked internal carotid artery—ophthalmic artery aneurysm, *Journal of Neurosurgery*, 99(3), 2003, 526-533.
[12] Jou, L.D., Wong, G., Dispensa, B., Lawton, M.T., Higashida, R.T., Young, W.L., Saloner, D., Correlation between lumenal geometry changes and hemodynamics in fusiform intracranial aneurysms, *American Journal of Neuroradiology*, 26(9), 2005, 2357-2363.
[13] Steinman, D.A., Milner, J.S., Norley, C.J., Lownie, S.P., Holdsworth, D.W., Image-based computational simulation of flow dynamics in a giant intracranial aneurysm, *American Journal of Neuroradiology*, 24(4), 2003, 559-566.
[14] Gerdroodbary, M.B., Salavatidezfouli, S., A predictive surrogate model based on linear and nonlinear solution manifold reduction in cardiovascular FSI: A comparative study, *Computers in Biology and Medicine*, 189, 2025, 109959.
[15] Barzegar Gerdroodbary, M., Salavatidezfouli, S., A predictive surrogate model of blood haemodynamics for patient-specific carotid artery stenosis, *Journal of the Royal Society Interface*, 22(224), 2025, 20240774.
[16] Sforza, D.M., Putman, C.M., Cebral, J.R., Hemodynamics of cerebral aneurysms, *Annual Review of Fluid Mechanics*, 41(1), 2009, 91-107.
[17] Fung YC. Biomechanics: mechanical properties of living tissues. 2nd ed. Boston: Springer; 1993.
[18] Rostamian, A., Fallah, K., Rostamiyan, Y., Alinejad, J., Application of computational fluid dynamics for detection of high risk region in middle cerebral artery (MCA) aneurysm, *International Journal of Modern Physics C*, 34(02), 2023, 2350019.
[19] Cebral, J.R., Mut, F., Weir, J., Putman, C.M., Association of hemodynamic characteristics and cerebral aneurysm rupture, *American Journal of Neuroradiology*, 32(2), 2011, 264-270.
[20] Sadeh, A., Kazemi, A., Bahramkhoo, M., Barzegar Gerdroodbary, M., Computational study of blood flow inside MCA aneurysm with/without endovascular coiling, *Scientific Reports*, 13(1), 2023, 4560.
[21] Ding, J., Valipour, P., Impacts of coiling technique on hemodynamic of the MCA aneurysms: Computational study, *International Journal of Modern Physics C*, 35(05), 2024, 2450057.
[22] Valipour, P., Effects of coiling embolism on blood hemodynamic of the MCA aneurysm: A numerical study, *Scientific Reports*, 12(1), 2022, 22029.
[23] Barzegar Gerdroodbary, M., Wang, X., A Computational Analysis of Sac Volume Effects on Hemodynamics and Rupture Risk in Cerebral Saccular Aneurysms, *Journal of Applied and Computational Mechanics*, 2026, DOI: 10.22055/jacm.2025.48445.5236.
[24] Ali, R., Hassan, H.I., Sharma, A., Dhawan, A., Sharma, P., Taher, W.M., Alwan, M., Al-Hussainy, A.F., Mushtaq, H. and Heaie, T., Efficiency of endovascular coiling on the evolution of MCA cerebral aneurysm by hemodynamic analysis: Computational study, *International Journal of Modern Physics C*, 2025, 2550065.
[25] Haie, T., Ali, R., Albadr, R.J., Sharma, A., Dhawan, A., Sharma, P., Taher, W.M., Alwan, M., Jawad, M.J., Mushtaq, H., Computational analysis of equivalent porous conditions in realistic coiling techniques for hemodynamic evaluation of ICA aneurysms, *International Journal of Modern Physics C*, 2025, 2550029.
[26] AneuriskWeb project website, http://ecm2.mathcs.emory.edu/aneuriskweb, Emory University, Department of Math & CS, 2012
[27] Ansys, I., ANSYS® Fluent User's Guide, Release 2020 R2. Canonsburg: ANSYS, 2020.
[28] Voss, S., Beuing, O., Janiga, G., Berg, P., Stent-induced vessel deformation after intracranial aneurysm treatment–A hemodynamic pilot study, *Computers in Biology and Medicine*, 111, 2019, 103338.
[29] Qin, S., Wu, B., Liu, J., Shiu, W.S., Yan, Z., Chen, R., Cai, X.C., Efficient parallel simulation of hemodynamics in patient-specific abdominal aorta with aneurysm, *Computers in Biology and Medicine*, 136, 2021, 104652.
[30] Xu, L., Liang, F., Zhao, B., Wan, J., Liu, H., Influence of aging-induced flow waveform variation on hemodynamics in aneurysms present at the internal carotid artery: A computational model-based study, *Computers in Biology and Medicine*, 101, 2018, 51-60.
[31] Boccadifuoco, A., Mariotti, A., Celi, S., Martini, N., Salvetti, M.V., Impact of uncertainties in outflow boundary conditions on the predictions of

hemodynamic simulations of ascending thoracic aortic aneurysms, *Computers & Fluids*, 165, 2018, 96-115.
[32] Mitsos, A.P., Kakalis, N.M., Ventikos, Y.P., Byrne, J.V., Haemodynamic simulation of aneurysm coiling in an anatomically accurate computational fluid dynamics model, *Neuroradiology*, 50(4), 2008, 341-347.
[33] Malvè, M., Chandra, S., García, A., Mena, A., Martínez, M.A., Finol, E.A., Doblaré, M., Impedance-based outflow boundary conditions for human carotid haemodynamics, *Computer Methods in Biomechanics and Biomedical Engineering*, 17(11), 2014, 1248-1260.

ORCID iD

Mostafa Barzegar Gerdroodbary https://orcid.org/0000-0002-8243-9476
Li-Cai Zhao https://orcid.org/0009-0009-6429-9842

How to cite this article: Barzegar Gerdroodbary M., Zhao L. Investigation of Pulsatile Blood Flow Dynamics in Anterior Cerebral Artery Aneurysms under Different Physiological Conditions: Hemodynamic Analyses, *J. Appl. Comput. Mech.*, 12(3), 2026, 1093-1105. https://doi.org/10.22055/jacm.2025.48336.5158